Volume 1 | Number 1 | Jan 2013 | Pages 1–100

Journal of
Materials Chemistry A

Materials for energy and sustainability
www.rsc.org/materialsA

Li⁺
e⁻
e⁻
Li⁺
Li⁺
Li⁺

ROYAL SOCIETY
OF CHEMISTRY

This is an *Accepted Manuscript*, which has been through the Royal Society of Chemistry peer review process and has been accepted for publication.

Accepted Manuscripts are published online shortly after acceptance, before technical editing, formatting and proof reading. Using this free service, authors can make their results available to the community, in citable form, before we publish the edited article. We will replace this *Accepted Manuscript* with the edited and formatted *Advance Article* as soon as it is available.

You can find more information about *Accepted Manuscripts* in the **Information for Authors**.

Please note that technical editing may introduce minor changes to the text and/or graphics, which may alter content. The journal's standard **Terms & Conditions** and the **Ethical guidelines** still apply. In no event shall the Royal Society of Chemistry be held responsible for any errors or omissions in this *Accepted Manuscript* or any consequences arising from the use of any information it contains.

Enhanced Activity, Durability and Anti-poisoning property of Pt/W$_{18}$O$_{49}$ for Methanol Oxidation with a Sub-stoichiometric Tungsten Oxide W$_{18}$O$_{49}$ Support

Fan Li[1*], Hongyu Gong[1], Yan Wang[1], Hui Zhang[2*], Yizhi Wang[1], Shengnan Liu[2], Shuo Wang[2], Chunwen Sun[3*]

1. Beijing Key Laboratory for Green Catalysis and Separation, College of Environmental and Energy Engineering, Beijing University of Technology, Beijing 100124, China
2. School of Science, Beijing Jiaotong University, Beijing 100044, China
3. Key Laboratory for Renewable Energy, Beijing Key Laboratory for New Energy Materials and Devices, Beijing National Laboratory for Condensed Matter Physics, Institute of Physics, Chinese Academy of Sciences, Beijing 100190, China

Abstract

In this work, sub-stoichiometric tungsten oxide W$_{18}$O$_{49}$ was first studied as a support for a Pt catalyst. Metallic monoclinic W$_{18}$O$_{49}$ nanorods (NRs) with an isotropic morphology can not only improve electron, reactant, and product transport but can also enhance the utilisation of Pt for the methanol oxidation reaction (MOR). The specific activity for the forward peak (I$_f$) of Pt/W$_{18}$O$_{49}$ was determined to be 1.14 mA·cm$^{-2}_{Pt}$, that is approximately 1.4 and 1.8 times higher than that of the Pt-black and Pt/C, respectively. On the other hand, the robust W$_{18}$O$_{49}$ NRs improve the stability of Pt/W$_{18}$O$_{49}$. After a 5000-cycle accelerated durability test, the electrochemical surface area (ECSA) loss rate of Pt/W$_{18}$O$_{49}$ was only 27.12%, less than that of Pt-black and Pt/C. Additionally, numerous oxygen vacancies and two valence states of W (W^{5+} and W^{6+}) were found to co-exist in W$_{18}$O$_{49}$, which may promote hydrogen spillover and oxygen buffering. These effects together contributed to improve the anti-poisoning of Pt/W$_{18}$O$_{49}$ for the intermediates in MOR. The peak current ratio of the forward versus the backward (I$_f$/I$_b$) reaction is 1.12 for the Pt/W$_{18}$O$_{49}$, 0.99 for the Pt-black, and 0.79 for the Pt/C. It was found that the Magnéli phase W$_{18}$O$_{49}$ may be a promising catalyst support for MOR.

1. Introduction

Platinum (Pt) is considered to be a state-of-the-art catalyst in the anode electro-oxidation of small organic molecules (methanol, formic acid, etc.) for fuel cells.[1,2] However, several important issues need to be addressed before commercialisation. In addition to the cost challenges of Pt-based catalysts, another major difficulty is the sluggish kinetics for the methanol oxidation reaction (MOR) of Pt-based anode catalysts in direct methanol fuel cells (DMFCs), which result from the self-poisoning caused by strongly adsorbed intermediate species, such as CHO and CO, and so on.[4-6] To circumvent this problem, in the last decade, different types of co-catalytic elements, such as Ru,[7,8] Ce,[9,10] Mo[11,12] and W,[13,14] have been studied for incorporation into Pt catalysts. The presence of second and/or third elements in Pt-based catalysts could improve the MOR kinetics via a bi-functional mechanism or synergistic effect. Unfortunately, both the large negative redox potential of the Mo^{n+}/Mo^{0} couple and the low miscibility of Pt and Ce in the PtMe alloy limit the development of anti-poisoning Pt-based alloy catalysts.[15,16] Recently, numerous studies have shown that different types of tungsten oxide-supported Pt nanocomposite catalysts also show superior CO-tolerance.[17-20]

Magnéli phase $W_{18}O_{49}$, a novel sub-stoichiometric tungsten oxide, is of special interest due to its unique oxygen defect structure and promising properties. In recent years, monoclinic $W_{18}O_{49}$ has been widely applied in photocatalysis, water treatment, electrochromic fields, and so on.[21-23] However, there was no report found on its application as a support for a Pt catalyst in fuel cells. Monoclinic $W_{18}O_{49}$ consists of an ordered 2D lattice of edge-sharing distorted WO_6 octahedra, forming a 3D structure of pentagonal columns interspersed with hexagonal channels (Fig. S1, Supporting Information). Therefore, $W_{18}O_{49}$ nanorods (NRs) are not only highly anisotropic but also possess numerous oxygen vacancies or defects.[24-26] Actually, the anisotropy of

1D $W_{18}O_{49}$ NRs, like carbon nanotubes, can improve mass transport and the utilisation of a catalyst.[27] This is also the reason that $W_{18}O_{49}$, an electronic conductor, is more suitable as a support of Pt catalysts than the semiconductor of WO_3.[28] It has previously been demonstrated that sub-stoichiometric $W_{18}O_{49}$ exhibits good electrochromic properties upon interacting small ions, such as H^+, Li^+, and so on.[29,30] The tungsten bronze compound (H_xWO_y) causes a hydrogen spillover effect to strip the surface of Pt nanoparticles effectively in the MOR. X-ray photoelectron spectroscopy (XPS) studies indicate that two valence states of tungsten, W^{5+} and W^{6+}, co-exist in $W_{18}O_{49}$, and the charge transfer between them is believed to be closely linked to the polarisation transfer.[27,31] Kim and co-workers[23] demonstrated more oxygen vacancies in $W_{18}O_{49}$ NRs containing more W^{5+} ions. In this way, a postulated oxygen buffering effect of $W_{18}O_{49}$ NRs could enrich O_{ads} species at the surface of Pt catalysts and act as a nanostructured oxygen reservoir (Fig. S2). Both the hydrogen spillover effect and the oxygen buffering effect would significantly improve the electrocatalytic activity and anti-poisoning property of the $Pt/W_{18}O_{49}$ nanocomposite catalyst for MOR.

In addition to a highly electrocatalytic activity, the long-term durability of a Pt catalyst is still a key challenge that must be addressed before the commercialisation of DMFCs.[32,33] Up to now, highly dispersed Pt nanoparticles (NPs, 2-5 nm) on an amorphous carbon support (Pt/XC-72) represented the most widely used commercial catalyst. Many reported studies have shown that electrochemical corrosion of carbon supports causes dissolution/aggregation/Oswald ripening of the Pt NPs, which results in the loss of the electrochemical surface area (ECSA) and degradation of the activity of the catalyst.[34-36] Therefore, more robust non-carbon supports, such as conductive metal oxide, are needed.[37] A series of sub-stoichiometric metal oxide supports, in Magnéli phase[28,38,39] ($W_{18}O_{49}$, Ti_4O_7, Mo_4O_{11}) with good electronic conductivity, has shown a novel potential support for Pt-based catalysts. Based on the results of our previous studies on Ti_4O_7[40] as a durable support, in this work, we designed $W_{18}O_{49}$ NRs support Pt NPs for small organic molecule electro-oxidation.

2. Experimental

2.1 Synthesis of the $W_{18}O_{49}$ support

The synthesis method is similar to that reported by Guo and co-workers.[26] In a typical synthesis, $W_{18}O_{49}$ NRs were synthesised by pyrolysing the $(NH_4)_xWO_{3+x/2}$ nanorod precursor at 600 °C for 1 h under a 5 vol.% H_2/Ar flow. The nanorod precursor was prepared by a hydrothermal reaction as follows. Sodium Tungstate Dihydrate ($Na_2WO_3 \cdot 2H_2O$, 1.6493 g, MW=329.86, Tianjin Fu Chen Chemical Reagents Factory) and Ammonium sulphate ($(NH_4)_2SO_4$, 1.3214 g, MW=132.14, Sinopharm Chemical Reagent Co. Ltd) were dissolved in 50 ml of de-ionised water under stirring in a 100 ml Teflon-lined stainless autoclave. The pH value of the solution was then adjusted drop-wise to 1.5 by adding a 3 M HCl solution and then hydrothermally treated at 200 °C for 24 h. After natural cooling, the product was collected by centrifugation (10000 rpm) and washed repeatedly with de-ionised water and ethanol followed by vacuum drying at 60 °C for 12 h.

2.2 Synthesis of Pt/$W_{18}O_{49}$ nanocomposite catalyst

Eighty milligrams of the as-prepared $W_{18}O_{49}$ NRs was dispersed in 50 mL of glycol with an ultrasonic wave. Subsequently, 31 mg of cis-Diamminedichloro platinum ($PtCl_2(NH_3)_2$, MW=300.06, Alfa Aesar, A Johnson Matthey Company) was added into the suspension and was further stirred for 2 h under ambient conditions. After refluxing at 145 °C for 2 h, the suspension was cooled down to room temperature naturally. The catalysts were collected by centrifugation (10000 rpm) and washed repeatedly with de-ionised water and ethanol. Finally, the nanocomposite Pt/$W_{18}O_{49}$ catalyst was dried at 80 °C for 10 h under vacuum.

2.3 Characterisations of materials

The crystalline phases of the $W_{18}O_{49}$ NRs support and Pt/$W_{18}O_{49}$ nanocomposite catalyst were characterised by X-ray powder diffraction (XRD) analysis (D8 Advance, Bruker, Karlsruhe, Deutschland). Morphologies were observed by scanning electron microscope (SEM, Hitachi S-4300, Tokyo, Japan). Transmission electron microscope (TEM) and high resolution transmission electron microscope (HRTEM) images of Pt/$W_{18}O_{49}$ were taken with JEOL JEM2100/JEM2100F (TEM, JEOL JEM2100/ JEM2100F, Tokyo, Japan). The surface properties and electronic structure of the

catalysts were evaluated by XPS with Al Kαradiation (Kratos AXIS Ultra DLD, Manchester Britain). The binding energy was calibrated with the C1s position of carbon support at 284.80 eV. The compositions of the catalysts were determined by inductively coupled plasma atomic emission spectrometry (ICP-AES, Thermo Fisher, IRIS Intrepid ER/S, Waltham, USA).

2.4 Electrochemical measurements

Glassy carbon (GC) electrodes were polished with alumina powder, ultrasonically washed, and blow dried, successively, before being dropped in catalyst ink. Based on the ICP-AES measurement, $Pt/W_{18}O_{49}$, Pt-black (Hispec 1000, Johnson Matthey) and Pt/C (Hispec3000, Johnson Matthey) were diluted to 1.3 mg·mL^{-1}, 1.5 mg·mL^{-1} and 1.4 mg·mL^{-1}, respectively, with a 0.05 wt% ethanol diluted Nafion solution. Then, 10 μl of the above three suspensions were transferred onto the polished GC electrode substrates. Before testing, the electrodes were solidified for 0.5 h under ambient conditions.

Electrochemical measurements were performed by cyclic voltammetry (CV, VMP3, Bio-Logic SA). The GC electrode (Ø 5 mm) with an area of 0.196 cm^2 was used as the working electrode. A Pt foil (10×10×0.3 mm) and a saturated calomel electrode (SCE) were used as the counter electrode and the reference electrode, respectively. Cyclic voltammetry measurements were carried out in an Ar-purged 0.5 M H_2SO_4 solutions at a sweep rate of 50 mV·s^{-1}. ECSA was calculated based on equation (1) as follows:

$$ECSA = \frac{Q_H}{0.21[Pt]} \quad (1)$$

where the correlation constant of 0.21 (mC·cm^{-2}) represents the charge required for monolayer adsorption of hydrogen on a Pt surface. $[Pt]$ is the Pt loading (mg·cm^{-2}) on the electrode, and Q_H is the amount of charge exchanged during the adsorption of hydrogen atoms on Pt (mC·cm^{-2}).

MOR measurements were performed in a 0.5 M H_2SO_4 and 0.5 M CH_3OH solution at a sweep rate of 50 mV·s^{-1} under ambient atmospheric conditions. Accelerated

durability tests (ADT) were performed in an Ar-purged 0.5 M H_2SO_4 solutions at a sweep rate of 100 $mV \cdot s^{-1}$ for 5000 cycles.Chronoamperometry measurements were performed in a 0.5 M H_2SO_4 and 0.5 M CH_3OH solution after a 50-cycle CV activity in an Ar-purged 0.5 M H_2SO_4 solution with a sweep rate of 100 $mV \cdot s^{-1}$. First, the GC electrode loaded with Pt catalysts was held at 0.509 V (vs. SCE) for 1.0 s to oxidize completely any adsorbate to obtain a clean surface; second, the potential was then stepped negatively to -0.441 V (vs. SCE) and stayed for 5 s to restore the solution near electrode surface; Finally, the potential was keep at 0.359 V (vs. SCE) to oxidize methanol and transient current–time (0~100 s) curve of CH_3OH oxidation was recorded. After a 5000-cycle ADT, chronoamperometry measurements were also performed as the above process. For CO stripping voltammetry, CO gas was purged into the solution at a position close to the working electrode for 1 s to 40 s, with the electrode polarized at -0.191 V (vs. SCE) in a fume hood. The excess CO was purged with Ar for 30 min under potential control followed by CO stripping at a scan rate of 50 $mV \cdot s^{-1}$.

3. Results and discussion

3.1 Crystalline phase analysis

The crystallinity and purity of the as-synthesised samples were investigated by XRD. Fig. 1a shows a typical XRD pattern of the $W_{18}O_{49}$ NRs support. All of the peaks in this pattern can be indexed to a monoclinic $W_{18}O_{49}$ phase, as shown in the inset of Fig. 1a. No peaks from any other materials were found in the obtained sample, revealing the formation of pure phase $W_{18}O_{49}$. As shown in Fig. S3, there are two broad characteristic bands located at approximately 100-400 cm^{-1} and 600-900 cm^{-1} in the Raman spectrum, which result from the wide range of W-O-W bond lengths within the $W_{18}O_{49}$ phase. This result agrees well with the results of other groups,[41,42] which also confirms that the as-prepared sample consists of pure $W_{18}O_{49}$ NRs. The highest intensity of the (010) suggests that the possible crystal growth of the $W_{18}O_{49}$ NRs is [010], which will be further demonstrated by the direct observation of the TEM (Fig. 2a). As shown in Fig. 1b, both $W_{18}O_{49}$ and Pt are detected in the XRD

pattern of the Pt/$W_{18}O_{49}$ nanocomposite catalyst. The highly dispersed Pt NPs on the surface of the $W_{18}O_{49}$ NRs appear like sesame seeds on a sausage, as is schematically shown in the inset of Fig. 1b and is also clearly shown in the TEM image (Fig. 3a).
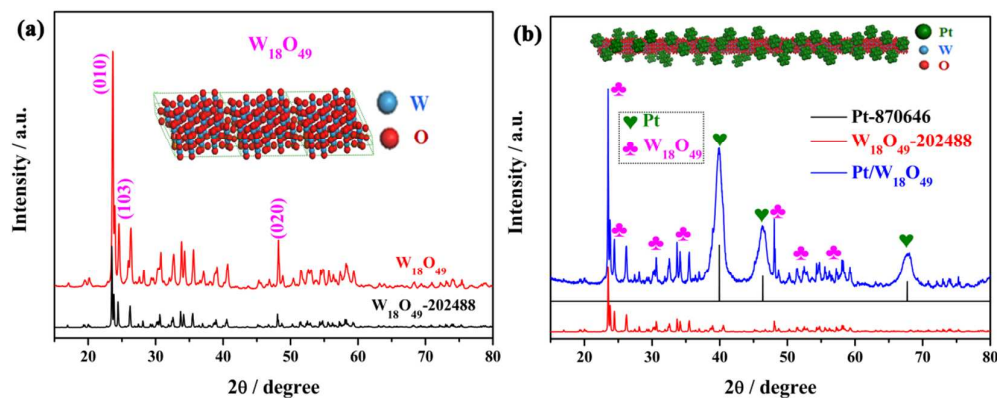

Fig. 1 X-ray powder diffraction (XRD) patterns: (a) $W_{18}O_{49}$ nanorods (NRs) support, inset: atomic structure of the monoclinic $W_{18}O_{49}$; (b) Pt/$W_{18}O_{49}$ nanocomposite catalyst, inset: schematic illustration of the Pt nanoparticles/$W_{18}O_{49}$ nanorod.

3.2 Morphological analysis of $W_{18}O_{49}$ NRs

The size and morphology of the products were examined by SEM and TEM. Fig. S4a shows that as-synthesised $W_{18}O_{49}$ is composed of many $W_{18}O_{49}$ NRs. Fig. 2a presents a typical TEM image of the $W_{18}O_{49}$ NRs observed by SEM. TEM observation and the selected area electron diffraction (SAED) pattern recorded along the longitudinal axis [010] direction revealed that the nanorod was single-crystalline $W_{18}O_{49}$ with a monoclinic structure. HRTEM in Fig. 2b shows that there are two sets of parallel fringes, with the lattice spacing of 3.78 Å and 3.73 Å (the inset of Fig. 2b) corresponding to the (010) and (103) planes of monoclinic $W_{18}O_{49}$, respectively.[43]
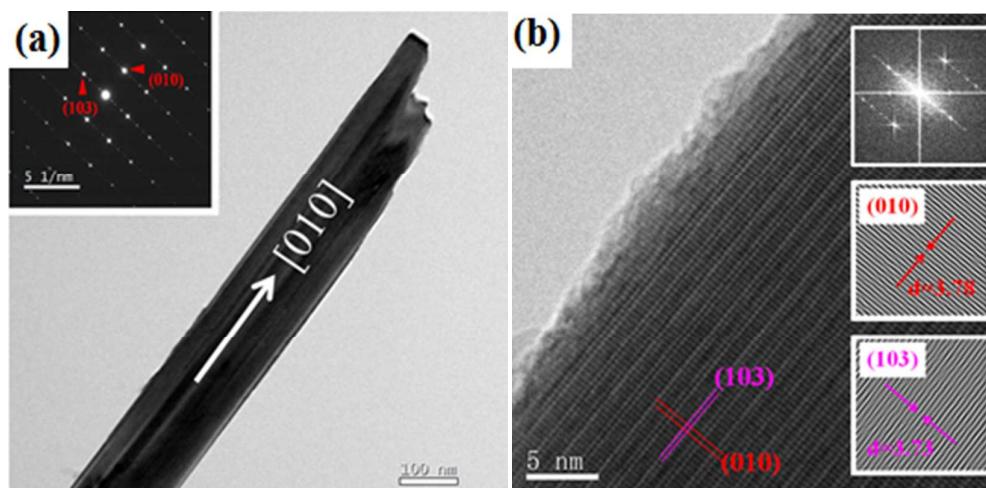
Fig. 2 (a) Transmission electron microscope (TEM) image of the $W_{18}O_{49}$ NRs support and the selected area electron diffraction (SAED) pattern shown in the inset;(b) High-resolution transmission electron-microscope (HRTEM) images of the $W_{18}O_{49}$ NRs, with a Fourier-transformed (FT) pattern and two inverse fast Fourier-filtered FT (IFFT) images in the inset.

3.3 Morphological analysis of the Pt/$W_{18}O_{49}$ composite

Fig. S4b shows a representative SEM image of the Pt/$W_{18}O_{49}$ nanocomposite catalyst prepared by a popular wet chemical reduction method. Further, one of the Pt/$W_{18}O_{49}$ is shown in Fig. 3a, and two patterns simultaneously appear in the SAED image (the inset of Fig. 3a). Orderly dispersed spots are indexed as monoclinic $W_{18}O_{49}$, and the rings belong to the dispersed Pt-NPs.[44] To further investigate the bonding of $W_{18}O_{49}$ and Pt-NPs, high-magnification TEM and HRTEM are employed. Fig. 3b shows an enlarged image of Fig. 3a, which clearly shows the Pt-NPs dispersed on the surface of the $W_{18}O_{49}$ NR, like sesame seeds on a sausage. As shown in Fig. 3c, the size of the Pt-NPs is approximately 8.30±1.57 nm. The lattice fringes of 0.227 nm for the Pt-NPs supported on the $W_{18}O_{49}$ NRs correspond to the Pt (111) plane in Fig. 3d. The (010) plane of the $W_{18}O_{49}$ NR support is detected in Fig. 3e along the [010] direction. Two FT patterns (inset in Fig. 3d and 3e) also further prove these observations.
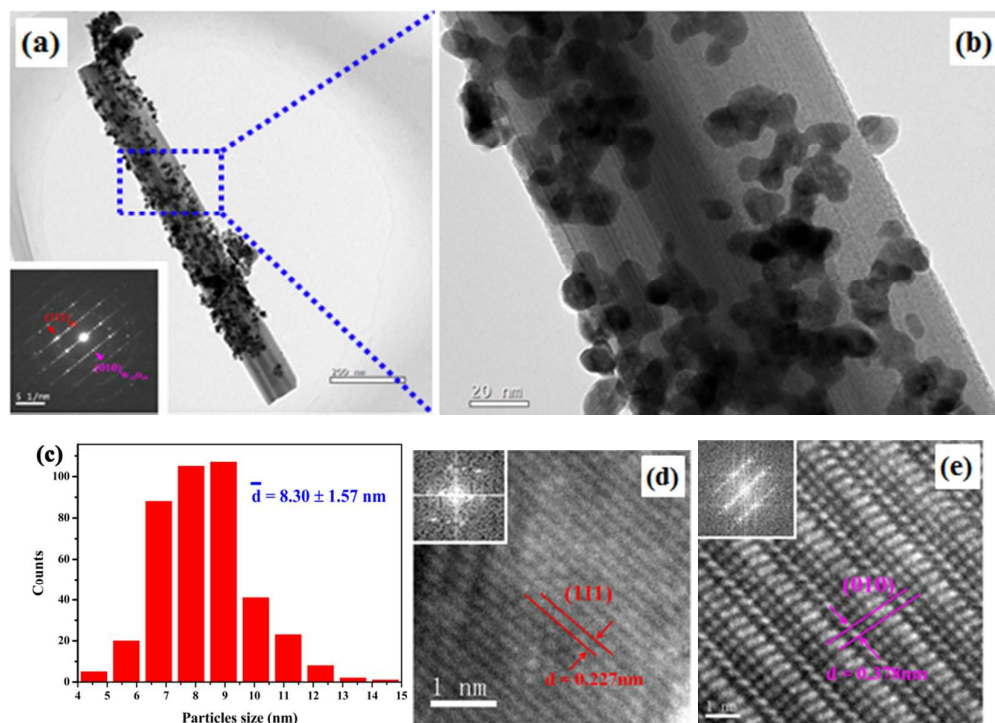
Fig. 3 (a) TEM image of the Pt/$W_{18}O_{49}$ composite and the SAED pattern shown in the inset; (b) high-magnification TEM image of the area marked in Fig. 3a;(c) the corresponding particle size distribution obtained by counting 400 particles in the TEM images;(d) HRTEM image of the Pt-NPs in Fig. 3b, with a FT pattern shown in the inset;(e) HRTEM image of the $W_{18}O_{49}$ NRs support in Fig. 3b, with a FT pattern shown in the inset.

3.4 Oxidation state analysis

XPS was used to examine the composition and valence state of Pt and Mo in Pt/$W_{18}O_{49}$ and Pt-black. The Pt 4f spectra of Pt/$W_{18}O_{49}$ (red) and Pt-black (black) are shown in Fig. 4a. Compared to the binding energy of the Pt 4f of the Pt-black (71.24 eV), the peak of Pt 4f in Pt/$W_{18}O_{49}$ shifts to a slightly higher value of 71.83 eV, indicating that an interaction exists between Pt and the $W_{18}O_{49}$ NRs support. This shift might be considered to be due to a strong metal-support interaction effect.[45] The strong interaction may promote the electron, proton, and oxygen transfer rate between the Pt NPs and $W_{18}O_{49}$ NRs support, which may enhance the catalytic activity of Pt/$W_{18}O_{49}$. Fig. 4b shows the deconvolution result of the W4f peaks of the $W_{18}O_{49}$ NRs support. The W4f$_{7/2}$ signals at 33.90 eV and 35.64 eV are assigned to W^{5+} and

W^{6+}, respectively. This indicates that different states of W4f co-exist in $W_{18}O_{49}$. This could benefit the hydrogen spillover and oxygen buffering effects, which might contribute to the improved intermediate-tolerance and electrocatalytic activity of the $Pt/W_{18}O_{49}$ nanocomposite catalyst. Although the binding energy and intensities of the peaks of W4f in $Pt/W_{18}O_{49}$ were significantly changed before (Fig. 4c) and after (Fig. 4d) the ADT, these spectra were still well fit by the W^{5+} and W^{6+} states. All of the deconvolution statistics of W 4f are listed in Table S1, which could indicate the anti-poisoning and stability of $W_{18}O_{49}$ and/or $Pt/W_{18}O_{49}$ in the following electrochemical test.
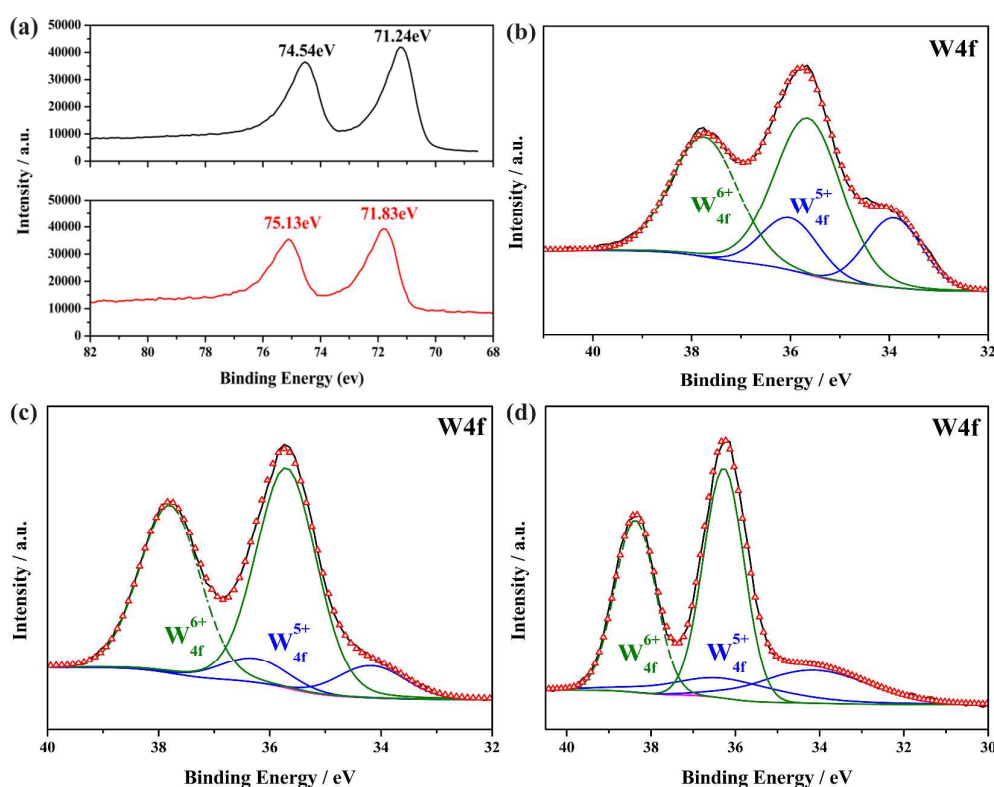

Fig. 4 (a) X-ray photoelectron spectroscopy (XPS) spectra of Pt 4f for $Pt/W_{18}O_{49}$ (red) and Pt-black (black);(b) W4f spectra for $W_{18}O_{49}$ NRs support and W 4f spectra of $Pt/W_{18}O_{49}$ before (c) and after (d) the accelerated durability tests (ADT).

3.5 Electrochemical behaviour of the $Pt/W_{18}O_{49}$ catalyst

Previous studies[17-20] have demonstrated that tungsten oxide (WO_3) modified Pt catalysts could enhance CO-tolerance for MOR. Fig. 5a shows the CV curves of $Pt/W_{18}O_{49}$ (purple curve), Pt-black (red curve), and Pt/C (blue curve) recorded at

room temperature in an Ar-purged 0.5 M H_2SO_4 solutions at a sweep rate of 50 mV·s^{-1}. The ECSA of the catalysts was calculated *via* equation (1), and Fig. 5b shows that ECSA of Pt/$W_{18}O_{49}$ (37.05 m^2·g^{-1}) is 1.59 times higher than that of Pt-black (23.28 m^2·g^{-1}). Although the $W_{18}O_{49}$ NRs support (green curve in Fig. 5d) had a particular amount of adsorption/desorption of hydrogen, the ECSA of $W_{18}O_{49}$ was 1.81 m^2·g^{-1} $W_{18}O_{49}$, which was ignored in compared with that of Pt/$W_{18}O_{49}$. These results indicate that $W_{18}O_{49}$ NRs can help to improve the dispersion and the activity of Pt. On one hand, $W_{18}O_{49}$ NRs play a role as carbonaceous supports to attach Pt NPs and to increase the active sites, like Pt/C; on the other hand, the hydrogen spillover effects may occur between the $W_{18}O_{49}$ NRs support and Pt NPs, which serves as a lower-energy pathway for H^+ to adsorb onto Pt and then diffuse to the $W_{18}O_{49}$ surface. There is a clear oxidation peak at approximately 0.1 V in the green circle of Fig. 5a and in a corresponding enlarged image in Fig. 5c below. According to previous studies, this peak is attributable to the Faradic process of the intercalation of hydrogen into tungsten oxide, and hydrogen tungsten bronzes of type $H_aWO_x(0 < a < 2)$ are formed.[46,47] We suggest four steps in the hydrogen spillover effect (insets in Fig. 5c): i) reactant, such as dissociated hydrogen atoms (H) from H_2 and CH_3OH, are chemically adsorbed on the Pt NPs surface; ii) hydrogen atoms are oxidised to cations, providing an extra electron for $W_{18}O_{49}$; iii) H^+ is transferred to the surface of $W_{18}O_{49}$ by a spillover mechanism; and iv) H^+ diffuses into the $W_{18}O_{49}$ lattice, reacts with the electron and the matrix neutralises the charge, which leads to the formation of H_aWO_x. The stoichiometric formula can be depicted as $WO_{49/18}$, where the hydrogen spillover occurs on the surface of the $WO_{49/18}$, as in equation (2).

$$(a-b)H^+ + (a-b)e^- + H_bWO_{49/18} \qquad H_aWO_{49/18} \quad (0 < b < a < 2) \qquad (2)$$

Thus, both the enhanced Pt dispersion by the $W_{18}O_{49}$ NRs support and the hydrogen spillover on the surface of $W_{18}O_{49}$ improved the ECSA of the Pt/$W_{18}O_{49}$ catalyst.
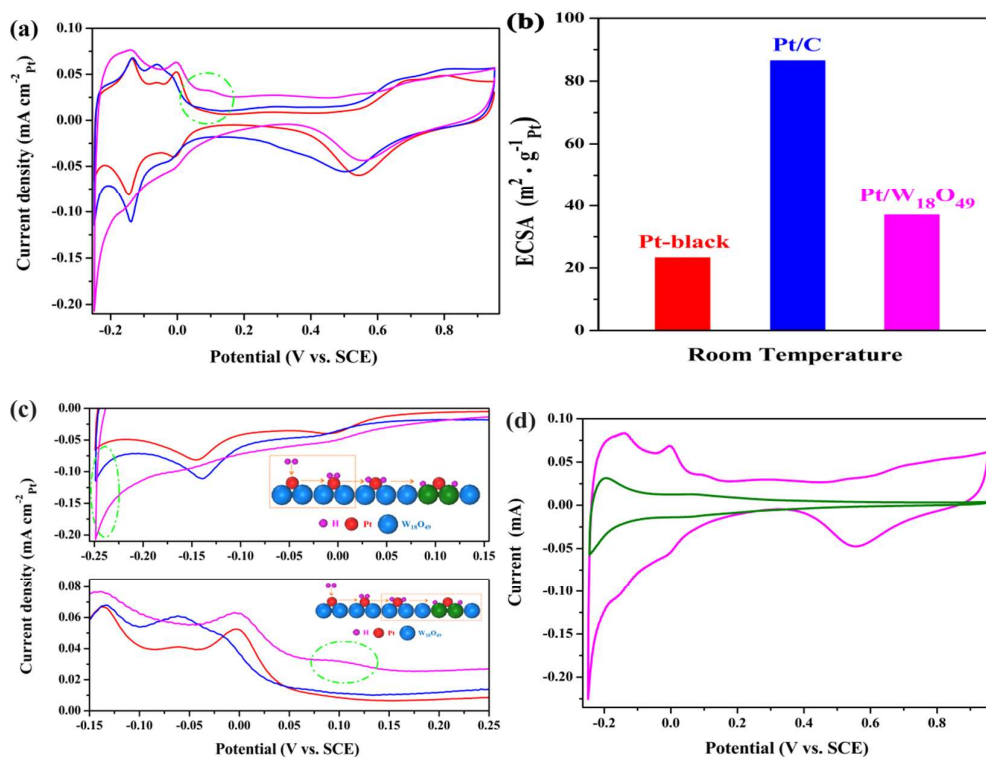
Fig. 5 Comparison of the electrocatalytic activities of Pt/$W_{18}O_{49}$, Pt/C and Pt-black. (a) CV curves recorded in an Ar-purged 0.5 M H_2SO_4 solution with a sweep rate of 50 mV·s^{-1} of Pt/$W_{18}O_{49}$ (purple curve), Pt-black (red curve) and Pt/C (blue curve);(b) Histogram of the specific ECSA of the three catalysts, respectively;(c) Enlarged images of the hydrogen absorption region (Fig. 5c top) and the green circle (Fig. 5c below) in Fig. 5a. As well as a schematic illustration of hydrogen spillover effect shown in inset, the green ball ($W_{18}O_{49}$) with the violate ball (H) form hydrogen tungsten bronzes of type $H_aWO_{49/18}$; (d) CV curves recorded in an Ar-purged 0.5 M H_2SO_4 solution with a sweep rate of 50 mV·s^{-1} of Pt/$W_{18}O_{49}$ (purple curve) and $W_{18}O_{49}$ (green curve); $W_{18}O_{49}$ loading was normalised to 10.4 μg for $W_{18}O_{49}$ and Pt/$W_{18}O_{49}$.

3.6 Electro-oxidation of small organic fuels

$W_{18}O_{49}$, as an outstanding electrochromic and/or optical material, has been researched widely.[23,24,31] As-synthesised $W_{18}O_{49}$ NRs show unusual photophysical properties, as indicated by the ultraviolet/visible (UV/Vis) absorption spectrum in Fig. S5. A large absorption tail presents in the visible and near infrared regions of the

spectrum, which confirms that $W_{18}O_{49}$ NRs consist of many oxygen vacancies.[25,48] The oxygen vacancies of the UV/Vis spectrum is consistent with the XPS results presented above of W^{5+} in $W_{18}O_{49}$. Furthermore, the existence of oxygen vacancies is beneficial to the adsorption and reaction of small molecules on the surface of $W_{18}O_{49}$ NRs, favouring the hydrogen spillover effect and/or the oxygen buffering effect. These enhance the utilisation and anti-poisoning of the $Pt/W_{18}O_{49}$ catalyst for MOR. The CV curves of MOR for $Pt/W_{18}O_{49}$ (purple curve), Pt-black (red curve), and Pt/C (blue curve) (Fig. 6a) showed that the forward peak current (I_f) of $Pt/W_{18}O_{49}$ (1.14 mA·cm^{-2}$_{Pt}$) is 1.41 times and 1.81 times larger than that of Pt-black (0.81 mA·cm^{-2}$_{Pt}$) and Pt/C (0.63 mA·cm^{-2}$_{Pt}$), respectively. Moreover, chronoamperomtric technique is an effective method to evaluate the electrocatalytic activity of different electrocatalystsat a state condition. Fig. S9a shows the transient current density curves of methanol oxidation by chronoamperometry experiments at 0.359 V (VS. SCE) for $Pt/W_{18}O_{49}$ (purple curve), Pt-black (red curve) and Pt/C (blue curve). The potential dependence of the steady-state current density recorded at 60 s of $Pt/W_{18}O_{49}$ (0.806 mA·mg^{-1}$_{Pt}$) is 1.81 times higher than that of Pt-black (0.445 mA·mg^{-1}$_{Pt}$) and similar to Pt/C (0.759 mA·mg^{-1}$_{Pt}$). These suggest that the kinetics of the MOR reaction catalysed by $Pt/W_{18}O_{49}$ is more effective. Fig. 6b shows that the forward peak potential (E_f) of $Pt/W_{18}O_{49}$ shifted to a lower value (0.654 V) compared with the potential of Pt-black (0.665 V) and Pt/C (0.689 V), which shows that the $Pt/W_{18}O_{49}$ catalytic dehydrogenation of methanol is thermodynamically easier. Although the onset potential of $Pt/W_{18}O_{49}$ is equivalent to that of Pt-black and Pt/C (0.1 V), the ratio of the forward peak current to the back peak current (I_f/I_b) is 1.12 for the $Pt/W_{18}O_{49}$, 0.99 for the Pt-black, and 0.79 for the Pt/C. These data in Table S2 indicate that $Pt/W_{18}O_{49}$ has the highest anti-poisoning property for the intermediates in the MOR among the three catalysts. Increasing the number and efficiency of active sites by the synergistic effect because of the interaction between Pt and $W_{18}O_{49}$ NRs support could promote spillover of the oxygen along their interface; this would enrich the O_{ads} species on the Pt surface, where $W_{18}O_{49}$ NRs act as a nanostructured oxygen reservoir.[49] The oxygen buffering effect in $Pt/W_{18}O_{49}$ is simulated in Fig. S2. $W_{18}O_{49}$ NRs function as

promoters by maintaining potential redox interfaces with active Pt NPs, which contributes to the formation of Pt-O$_{ads}$, promoting the oxidisation of intermediate species (such as Pt-CHO$_{ads}$, Pt-CO$_{ads}$, etc.) to H$_2$O and CO$_2$ in MOR and the regeneration of free Pt sites for the further oxidation of methanol. This explains the highly anti-poisoning property of the Pt/W$_{18}$O$_{49}$ catalyst for MOR.

Fig. 6c shows the formic acid oxidation reaction (FOR) curves of Pt/W$_{18}$O$_{49}$ (purple curve), Pt-black (red curve), and Pt/C (blue curve); the I_f of Pt/W$_{18}$O$_{49}$ (0.44 mA·cm$^{-2}_{Pt}$) is also higher than that of Pt-black (0.29 mA·cm$^{-2}_{Pt}$) and Pt/C (0.27 mA·cm$^{-2}_{Pt}$). This result also suggests that the Pt/W$_{18}$O$_{49}$ catalyst possesses the highest activity. Although the onset potential of Pt/W$_{18}$O$_{49}$ for FOR is equivalent to that of Pt-black and Pt/C (0.01 V), E_f of Pt/W$_{18}$O$_{49}$ was positively shifted (0.656 V) compared to the potential of the Pt-black and Pt/C (Table S2). Formic acid is a potential intermediate in MOR, for which a more positive E_f for FOR indicates a higher catalytic activity for MOR during its reverse sweep. In turn, it is confirmed that Pt/W$_{18}$O$_{49}$ is an effective anti-poisoning catalyst for MOR.
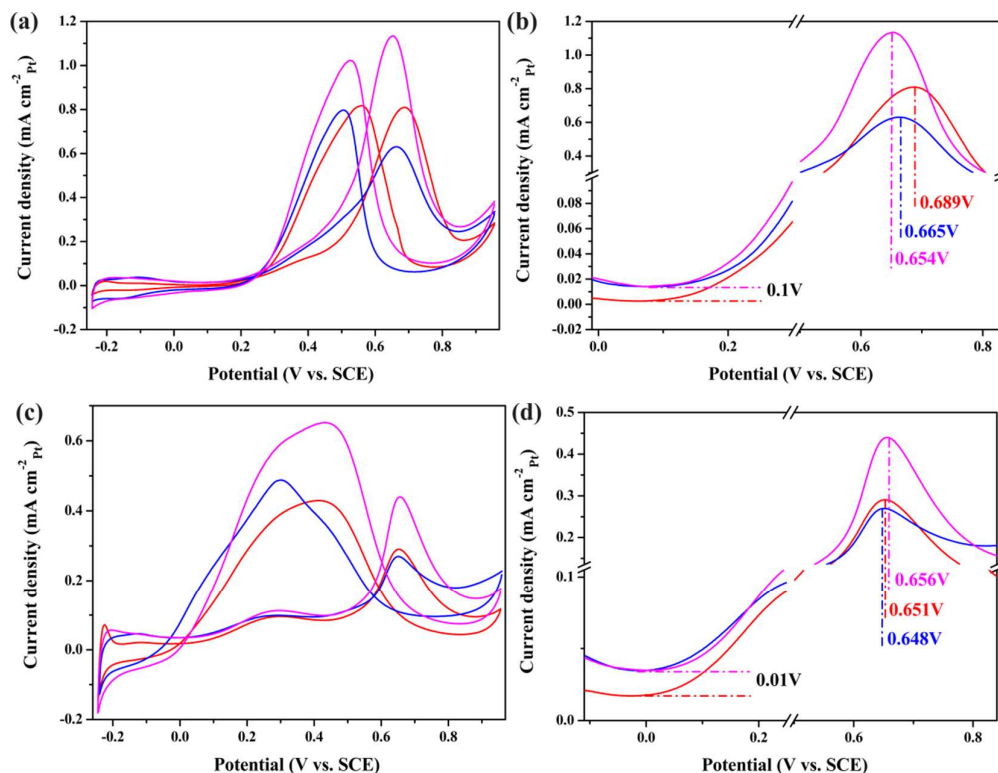

Fig. 6 (a) Methanol oxidation reaction (MOR) curves recorded under ambient

atmospheric conditions in a 0.5 M H_2SO_4 and 0.5 M CH_3OH mixed solution with a sweep rate of 50 mV·s^{-1} for Pt/W$_{18}$O$_{49}$ (purple curve), Pt-black (red curve) and Pt/C (blue curve); (b) enlarged image of the forward CV for MOR, including the on-set potential and the forward peak current density (I_f); (c) formic acid oxidation reaction (FOR) curves recorded under ambient atmosphere in a 0.5 M H_2SO_4 and 0.5 M CHOOH mixed solution with a sweep rate of 50 mV·s^{-1} of the Pt/W$_{18}$O$_{49}$ (purple curve), Pt-black (red curve) and Pt/C (blue); (d) enlarged image of the forward CV for FOR, including the on-set potential and the I_f.

3.7 CO stripping voltammograms of the electrocatalysts

The enhanced MOR activity and CO tolerance of the Pt/W$_{18}$O$_{49}$ catalyst was further studied with CO stripping voltammetry performed as a function of CO poisoning time in 0.5 M H_2SO_4 at room temperature with a sweep rate of 50 mV s^{-1}. Fig. 7 shows the CO stripping voltammograms for Pt/W$_{18}$O$_{49}$ and commercial Pt-black and Pt/C, respectively. A CO oxidation peak was observed for the commercial Pt-black around 0.50 V (Vs. SCE) after purging with pure CO gas for 1s, and the equilibrium CO coverage was reached within 6s (Fig. 7a). For the commercial Pt/C, the CO oxidation peak was observed at around 0.57 V (Vs. SCE) after 1s, and the equilibrium CO coverage was reached within 4s (Fig. 7b). However, for the Pt/W$_{18}$O$_{49}$ catalyst, CO oxidation peak appeared at about 0.49V (Vs. SCE) and the equilibrium CO coverage was reached after 30 s. The slowest CO adsorption rate among the three catalysts indicates that Pt/W$_{18}$O$_{49}$ has superior CO tolerance relative to the conventional Pt-black and Pt/C catalyst.
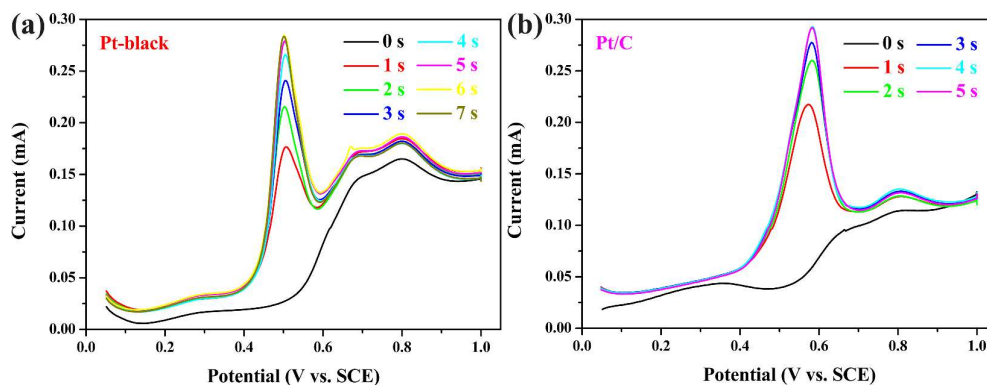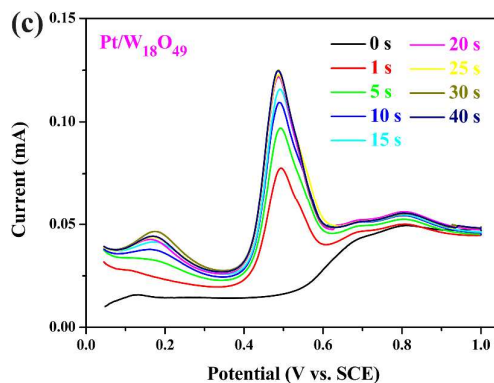
Fig. 7 CO stripping voltammograms of (a) Pt-black, (b) Pt/C and (c) Pt/W$_{18}$O$_{49}$ as a function of CO poisoning time. The sweep rate is 50 mV s^{-1}.

3.8 Synergistic effect in Pt/W$_{18}$O$_{49}$ catalysed MOR

W$_{18}$O$_{49}$ NRs as novel supports can provide various advantages for Pt-based catalysts used in fuel cells. First, W$_{18}$O$_{49}$ NRs, like carbon nanotubes, have an anisotropic morphology that can improve mass transport and the utilisation of catalyst, as previously described; second, the charge carrier concentration of Magnéli phase W$_{18}$O$_{49}$ is approximately 1.87×10^{22} cm^{-3},[28] which can provide adequate electronic conductivity for supported Pt catalyst and reduce the ohmic polarisation of the electrode catalyst. Additionally, a unique synergistic effect of the Pt/W$_{18}$O$_{49}$ composite, including the hydrogen spillover effect and oxygen buffering effect, improves the electro-oxidation of small organic fuels (methanol, formic acid) effectively. Thus, the Pt/W$_{18}$O$_{49}$ composite catalyst shows higher anti-poisoning for the intermediates in MOR than the commercial Pt-black and Pt/C catalysts. According to above the results of electrochemical testing, Fig. 8 schematically illustrates this synergistic effect: i) CH$_3$OH is chemically adsorbed on the Pt/W$_{18}$O$_{49}$ surface and then catalyses dehydrogenation to produce protons (H$^+$) and intermediates (Pt-CH$_3$O$_{ads}$, Pt-CH$_2$O$_{ads}$, Pt-CHO$_{ads}$, Pt-CO$_{ads}$, etc.). The oxygen vacancies (UV/Vis spectrum) within monoclinic W$_{18}$O$_{49}$ increase the number of W^{5+} states (XPS deconvolution), favouring the formation of H$_x$WO$_{49/18}$ and consequently enhancing the charge intercalation ability of W$_{18}$O$_{49}$ NRs. The hydrogen spillover effect will effectively promote the catalytic dehydrogenation of methanol. ii) Through the transformation between different valence states of tungsten, W$_{18}$O$_{49}$ NRs act as a

nanostructured oxygen reservoir, which could enrich the Pt NPs surface with O_{ads} species by a postulated oxygen buffering effect. iii) Throughout MOR, the oxygen buffering effect of Pt-O_{ads} can oxidise the hydrogen spillover effect of intermediates to H_2O and CO_2 and the regeneration of free Pt sites for further oxidation of methanol. The synergistic effect of the Pt/$W_{18}O_{49}$ remarkably improved the catalyst activity and anti-poisoning for MOR.
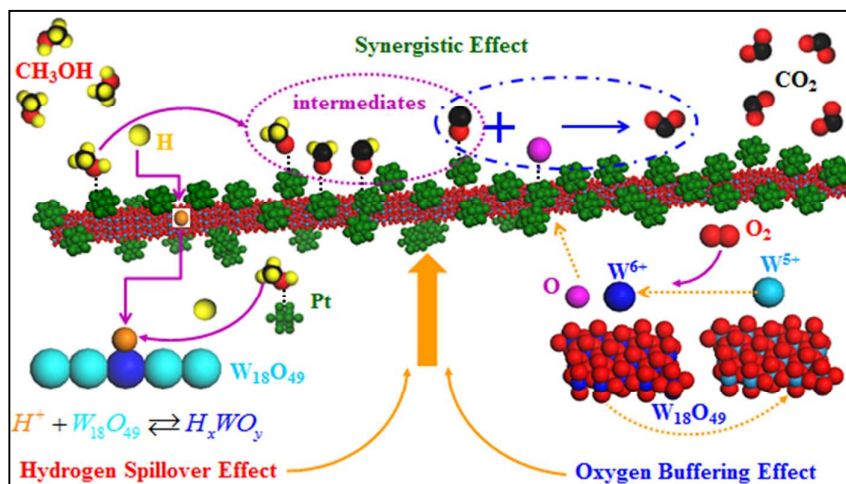

Fig. 8 Schematic illustration of the synergistic effect of Pt/$W_{18}O_{49}$ catalysing MOR, including the hydrogen spillover effect and the oxygen buffering effect.

3.9 Stability of the electrocatalysts

Stability is a critical criterion for evaluating the performance of an electrocatalyst. The ADTs were estimated by CV sweeps at 100 mV·s^{-1} in an Ar-purged 0.5 M H_2SO_4 solution at room temperature. The ECSAs of Pt/$W_{18}O_{49}$ (purple curve), Pt-black (red curve) and Pt/C (blue curve) are reduced with the increment of the CV circles, as shown in Figs. 9a and 9c (solid for the 1st cycle and dotted for the 5000th cycle, respectively). After 5000 cycles, the loss rate of Pt-black and Pt/C were found to be 49.50% and 85.25%, respectively (compared with 27.12% of the Pt/$W_{18}O_{49}$). The ECSA loss of Pt-black was attributed to the aggregation of the nanoparticles during the test and the TEM images of Pt-black before and after a 5000-cycle durability test, as show in Figs. S6a and S6b. As is well known, dissolution/aggregation/Oswald ripening of Pt NPs are the main factors to reduce the stability of Pt/C used in fuel cell operation. After 5000 cycles, Pt/C was obviously agglomerating and shedding, as

shown in the comparison of Figs. S6c and S6d. In this work, a Magnéli phase $W_{18}O_{49}$ is an attractive stable-support; there is a slight change for $W_{18}O_{49}$ NRs after a 5000-cycle test, as shown in Fig. S7. As a direct result, the stability of $Pt/W_{18}O_{49}$ is superior than that of Pt-black and Pt/C. One can see that there is almost no change $Pt/W_{18}O_{49}$ before and after ADT, as shown in Figs. S6e and S6f. The statistical results of Fig. 3c and Fig. S8 confirm that the Pt NPs size of $Pt/W_{18}O_{49}$ increased from 8.3 nm to 9.0 nm after a 5000-cycle ADT. The result of TEM is in accord with the result of the CV measurement, which demonstrates that the novel support of $W_{18}O_{49}$ NRs can effectively prevent the aggregation and Oswald ripening of Pt NPs in the electrochemical test to enhance the stability of the $Pt/W_{18}O_{49}$ catalyst. The chronoamperometry measurements date before and after a 5000-cycle ADT in Table S3 also confirmed the highest stability of $Pt/W_{18}O_{49}$ in the three catalysts. Fig. S9d shows the loss of transient current density at 60 s after the ADT of $Pt/W_{18}O_{49}$ (17.74%) is lower than that of Pt-black (Fig. S9b, 48.09%) and Pt/C (Fig. S9c, 72.46%). Therefore, all of these results support $W_{18}O_{49}$ as a new generation of stable support.
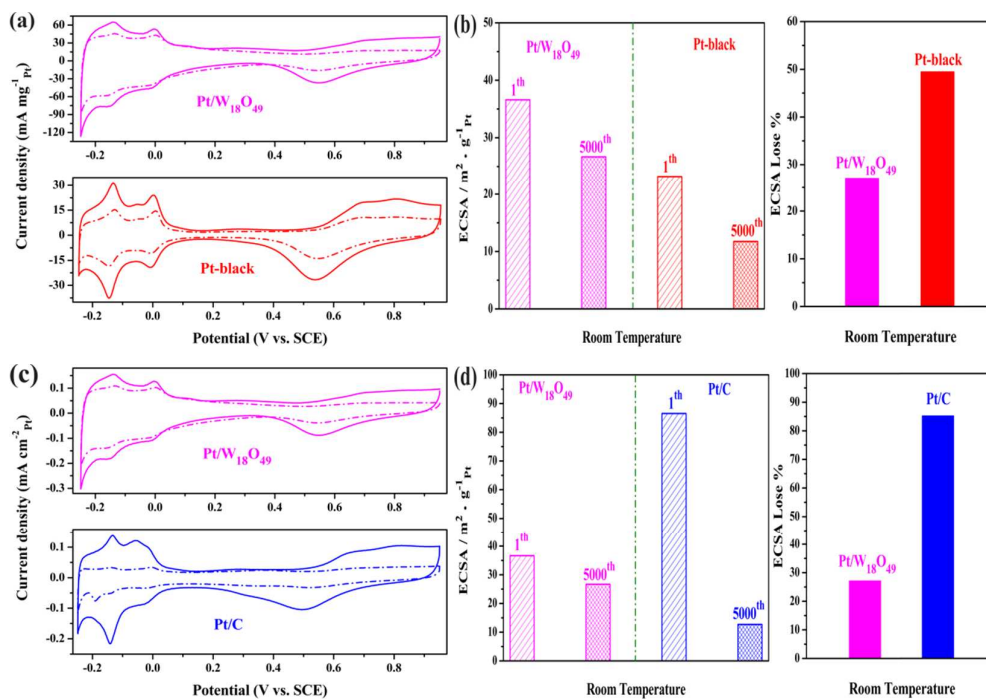

Fig. 9 (a) Accelerated durability tests (ADT) recorded in an Ar-purged 0.5 M H_2SO_4 with a sweep rate of 100 mV·s^{-1} of $Pt/W_{18}O_{49}$ (purple solid curve for the 1st cycle and dotted curve for the 5000th cycle), Pt-black (red solid curve for the 1st cycle and dotted

curve for the 5000th cycle) and Pt/C (blue curve); (b) left is the histogram of the specific ECSA and right is the ECSA loss of the Pt/W$_{18}$O$_{49}$ (purple curve) and Pt-black (red curve) before and after a 5000-cycle ADT, respectively; (c) ADT recorded in an Ar-purged 0.5 M H$_2$SO$_4$ with a sweep rate of 100 mV·s^{-1} of Pt/W$_{18}$O$_{49}$ (purple solid curve for the 1st cycle and dotted curve for the 5000th cycle) and Pt/C (blue solid curve for the 1st cycle and dotted curve for the 5000th cycle); (d) left is the histogram of the specific ECSA and right is the ECSA loss of the Pt/W$_{18}$O$_{49}$ (purple columns) and Pt/C (blue columns) before and after a 5000-cycle ADT, respectively.

4. Summary

In this work, sub-stoichiometric tungsten oxide W$_{18}$O$_{49}$, as an electronic conductor, was used as a catalyst support to load Pt NPs (Pt/W$_{18}$O$_{49}$), achieving higher catalytic activity, anti-poisoning and stability than the commercial Pt-black and Pt/C catalysts. XPS results revealed a strong metal-support interaction between Pt and W$_{18}$O$_{49}$ NRs; in addition, two valence states of W (W^{5+} and W^{6+}) were found to co-exist in W$_{18}$O$_{49}$, which may promote hydrogen spillover and oxygen buffering. These effects contributed to the improvement of the poisoning tolerance and the electrocatalytic activity of the Pt/W$_{18}$O$_{49}$ for MOR. Electrochemical test results suggest that the as-synthesised W$_{18}$O$_{49}$ NRs, like carbon nanotubes, not only have an anisotropic morphology that can improve mass transport and Pt utilisation but also have a robust and stable nature to enhance the stability of Pt/W$_{18}$O$_{49}$. Thus, the results obtained in this work demonstrated that the Magnéli phase W$_{18}$O$_{49}$ may be a promising catalyst support for MOR.

Acknowledgment

References

1 I. E. L. Stephens and I. Chorkendorff, *Angew. Chem. Int. Ed*, 2011, **50**, 1476-1477.

2 K. Yamamoto, T. Imaoka, W. J. Chun, O. Enoki, H. Katoh, M. Takenaga and A.

Sonoi, *Nature Chemistry*, 2009, **1**, 397-402.

3 B. Qiao, A. Wang, X. Yang, L. F. Allard, Z. Jiang, Y. Cui, J. Liu, J. Li and T. Zhang, *Nature Chemistry*, 2011, **3**, 634-641.

4 S. Pak, A. Wieckowski and M. J. Weaver, *J. Am. Chem. Soc.*, 2003, **125**, 2282-2290.

5 K. Miyazaki, Y. Nishida, K. Matsuoka, Y. Iriyama, T. Abe, M. Matsuoka, K. Kikuchi and Z. Ogumi, *Electrochemistry*, 2007, **75**, 217-220.

6 A. S. Aricò, S. Srinivasan and V. Antonucci, *Fuel Cell*, 2001, **1**,133-161.

7 S. Alayoglu, A. U. Nilekar, M. Mavrikakis and B. Eichhorn, *Nature Materials*, 2008, **7**, 333-338

8 Z. Liu, X. Y. Ling, X. Su and J. Y. Lee, *J. Phys. Chem.* B, 2004, **108**, 8234-8240.

9 R. G. Blas, C. L. Menéndez, C. A. Vélez, . R. Fachini, A. J. Peck, S. D. Senanayake, D, Stacchiola, K. Sasaki and C. R. Cabrera, *Smart Grid and Renewable Energy*, 2013, **4**, 1-9.

10 P. Malacrida, M. E. Escribano, A. V. Casadevall, I. E. L. Stephens and I. Chorkendorff, *J. Mater. Chem. A*, 2014, **2**, 4234-4243.

11 M. Götz and H. Wendt*, ElectrochimicaActa*, 1998, **43**, 3637-3644.

12 A. Miura, M. E. Tague,J. M. Gregorie, X. Wen, R. B. Dover, H. D. Abruña and F. J. Disalvo, *Chem. Mater.*, 2010, **22**, 3451-3456.

13 Y. Dai, Y. Liu and S. Chen, *ElectrochimicaActa*, 2013, **89**, 744-748.

14 G. S. Chai and J. S. Yu, *J. Mater. Chem.*, 2009, **19**, 6842-6848.

15 J. E. Hu, Z. Liu, B. W. Eichhorm and G. S. Jackson, *International Journal of Hydrogen Energy*, 2012, **37**, 11268-11275.

16 A. Janghorban, M. Lomello-Tafin, J. M. Moreau and P. Galez, *Intermetallics*, 2010, **18**, 2208-2218.

17 C. Yang, N. K. Van der Laak, K. Y. Chan and X. Zhang, *ElectrochimicaActa*, 2012, **75**, 262-272.

18 X. Cui, L. Guo, F. Cui, Q. He and J. Shi, *J. Phys. Chem. C*, 2009, **113**, 4134-4138.

19 Z. Zhao, Z. Yao, J. Zhang, R. Zhu, Y. Yu and Q. Li, *J. Mater. Chem.*, 2012, **22**, 16514-16519.

20 J. Zhang, J. Tu, G. Du, Z. Dong, Q. Su, D. Xie and X. Wang, *ElectrochimicaActa*,

2013, **88**, 107-111.

21 S. H. Baeck, K. S. Choi, T. F. Jaramillo, G. D. Stucky and E. W. Mcfarlanf, *Adv. Mater.*, 2003, **15**, 1269-1273.

22 X. Gao, F. Xiao, C. Yang, J. Wang and X. Su, *J. Mater. Chem. A*, 2013, **1**, 5831-5834

23 D. H. Kim, *Solar Energy Materials & Solar Cells*, 2012, **107**,81-86.

24 H. Zhou, Y. Shi, Q. Dong, Y. Wang, C. Zhu, L Wang, N. Wang, Y. Wei, S. Tao and T. Ma, *J. Mater. Chem. A*, 2014, **2**, 4347-4354.

25 G. Xi, S. Ouyang, P.Li, J.Ye，Q. Ma，N. Su，H. Bai and C. Wang, *Angew. Chem. Int. Ed.*, 2012, **51**, 2395-2399.

26 C. Guo, S. Yin, M. Yan, M. Kobayashi, M. Kakihana and T. Sato, *Inorg. Chem.*, 2012, **51**, 4763-4771.

27 S. Shi, X. Xue, P. Feng, Y. Liu, H. Zhao and T. Wang, *Journal of Crystal Growth*, 2008, **310**, 462-466.

28 D. B. Migas, V. L. Shaposhnikov and V. E. Borisenko, J. Appl. Phys., 2010, **108**, 0937141-6.

29 A. M.L. Cruz, L. M. T. Martínez, F. G. Alvarado, E. Morán and M. A. Alario-France, *Journal of Solid State Chemistry*, 2000,**151**, 220-224.

30 S. K. Deb, *Solar Energy Materials and Solar Cells*, 1992, **25**, 327-338.

31 C. Guo, S. Yin, Y. Huang, Q. Dong and T. Sato, *Langmuir*, 2011, **27**, 12172-12178.

32 S. Sun, G. Zhang, D. Geng, Y. Chen, R. Li, M. Cai and X. Sun, *Angew. Chem. Int. Ed.*, 2011, **50**, 422-426.

33 J. Zhang, K. Sasaki, E. Sutter and R. R. Adzic, *Science*, 2007, **315**, 220-222.

34 Y. Shao, G. Yin and Y. Gao, *Journal of Power Sources*, 2007, **171**, 558-566.

35 P. J. Ferreira, G. J. Ia O', Y. Shao-Horn, D. Morgan, R. Makharia, S. Kocha and H. A. Gasteiger, *Journal of The Electrochemical Society*, 2005, **152**, A2256-A2271.

36 Z. Peng and H. Yang, *J. Am. Chem. Soc.*, 2009, **131**, 7542-7543.

37 C. V. Subban, Q. Zhou, A. Hu, T. E. Moylan, F. T. Wagner and F. J. Disalvo, *J. Am. Chem. Soc.*, 2010, **132**, 17531-17536.

38 M. S. da Luz, A. de Campos, B. D. White and J. J. Neumeier, *Physical Review B*,

2009, **79**, 233106-1-233106-4.

39 M. Weissmann and R. Weht, *Physical Review B*, 2011, **84**, 1444191-4.

40 C. Yao, F. Li, X. Li and D. Xia, *J. Mater. Chem.*, 2012, **22**, 16560-16565.

41 D. Y. Lu, J. Chen, J. Zhou, S. Z. Deng, N. S. Xu and J. B. Xu, *J. Raman Spectrosc.*, 2007, **38**, 176-180.

42 F. Liu, T. Guo, Z. Xu, H. Gan, L. Li, J. Chen, S. Deng, N. Xu, D. Golberg and Y. Bando, *J. Mater. Chem. C*, 2013, **1**, 3217-3225.

43 Y. Li, Y. Bando and D. Golberg, *Adv. Mater.*, 2003, **15**, 1294-1286.

44 Y. Wang, L. Zhang, F. Li and B. Gu, *ElectrochimicaActa*, 2013, **102**, 1-7.

45 H. Zhang, C. Huang, R. Tao, Y. Zhao, S. Chen, Z. Sun and Z. Liu, *J. Mater. Chem.*, 2012, **22**, 3354-3359.

46 D. Wang, J. Li, X. Cao, G. Pang and S. Feng, *Chem. Commun.*, 2010, *46*, 7718-7720

47 J. Wang E. Khoo, P. S. Lee and J. Ma, *J. Phys. Chem. C*, 2009, **113**, 9655-9658.

48 G. Xi, J. Ye, Q. Ma, N. Su, H. Bai and C. Wang, *J. Am. Chem. Soc.*, 2012, **134**, 6508-6511.

49 R. Vellacheri, S. M. Unni, S. Nahire, U. K. Kharul and S. Kurungot, *ElectrochimicaActa*, 2010, **55**, 2878-2887.